

## **Removal and Degradation of Mixed Dye Pollutants by Integrated Adsorption-Photocatalysis Technique Using 2-D MoS<sub>2</sub>/TiO<sub>2</sub> Nanocomposite**

Gauthaman Chandrabose<sup>1</sup>, Avishek Dey<sup>1</sup>, Shivani Singh Gaur<sup>2</sup>, Sudhagar Pitchaimuthu<sup>3\*</sup>, Hema Jagadeesan<sup>2</sup>, N. St. John Braithwaite<sup>4</sup>, Vimalnath Selvaraj<sup>5</sup>, Vasant Kumar<sup>5</sup> and Satheesh Krishnamurthy<sup>1\*</sup>

<sup>1</sup>*School of Engineering and Innovation, The Open University, Milton Keynes, MK7 6AA, United Kingdom.*

<sup>2</sup>*PSG College of Technology, Coimbatore, Tamil Nadu 641004, India.*

<sup>3</sup>*Multi-Functional Photocatalyst and Coatings Group, SPECIFIC, College of Engineering, Swansea University (Bay Campus), Swansea, SA1 8EN, United Kingdom.*

<sup>4</sup>*School of Physical Sciences, The Open University, Milton Keynes, MK7 6AA, United Kingdom.*

<sup>5</sup>*Department of Materials Science and Metallurgy, University of Cambridge, Cambridge, CB3 0FS, United Kingdom*

*\*Corresponding authors:*

*Email:* [s.pitchaimuthu@Swansea.ac.uk](mailto:s.pitchaimuthu@Swansea.ac.uk) (SP); [satheesh.krishnamurthy@open.ac.uk](mailto:satheesh.krishnamurthy@open.ac.uk) (SK)

**Abstract:**

Two-dimensional (2D) Molybdenum disulfide ( $\text{MoS}_2$ ) has become one of the most exciting area of research for adsorbents due to its high surface area and abundant active sites. Mainly, 2D  $\text{MoS}_2$  show promising removal of textile dye pollutants by adsorption process, but it showed high affinity for anionic type dyes, that limits its performance in mixed dye pollutants treatment. Herein, we demonstrate an integrated approach to remove mixed dye pollutants (anionic and cationic) concurrently by combining adsorption and photocatalysis process. We synthesize  $\text{MoS}_2/\text{TiO}_2$  nanocomposites for different weight percentages 2.5, 5, 10, 20, 30, and 50wt% of pre-synthesized flower-like  $\text{MoS}_2$  nanoparticle by a two-step hydrothermal method. We demonstrate a new process of two-stage adsorption/photocatalysis using high wt % of  $\text{MoS}_2$  (Stage-I) and low wt% of  $\text{MoS}_2$  (Stage-II) nanocomposites. The proposed two-stage integrated adsorption and photocatalysis process using 50 % and 2.5% of  $\text{MoS}_2$  coated  $\text{TiO}_2$ , respectively showed complete removal of methylene blue dye ~5 times faster than conventional single-stage (adsorption or photocatalysis) water treatment process. Furthermore, the feasibility of the proposed two-stage method in mixed dye pollutants removal (anionic and cationic) testified, which showed excellent performance even in doubling the dye pollutant concentration. This work brings a deeper insight into understanding the morphology and concentration of 2-D  $\text{MoS}_2$  in  $\text{MoS}_2/\text{TiO}_2$  nanocomposite in tackling mixed dye pollutants and the possibilities of applying in textile dyeing industries wastewater treatment plants.

**Keywords:**  $\text{MoS}_2$ ,  $\text{TiO}_2$ , Adsorption, Photocatalysis, Dye Degradation, Water treatment.

**Introduction**

Today's globalization and growing population increases the demand of usage of textile products which relatively increases the usage of synthetic dyes. Resulting in release of high level of dyeing waste, polluting both land and freshwater resources. (Bhatia, 2017; Muthu, 2017)

Therefore it is very important to design a textile wastewater treatment plant having high efficiency in order to handle greater volume of wastewater discharge in a cost-effective way. In recent years, photocatalytic degradation of organic pollutants has been considered as a sustainable technology for wastewater treatment. (Vergili et al., 2012; Hermosilla et al., 2015; Kou et al., 2017; Park et al., 2017; Mehta et al., 2018; Li et al., 2020) The promise of photocatalytic degradation lies in the possibility of deployment in off-grid areas.

Titanium dioxide ( $\text{TiO}_2$ ) is the commonly employed photocatalyst for solar driven wastewater treatment.  $\text{TiO}_2$  is known for its promising properties like high stability, non-toxicity, cost effective and earth abundance oxide. However, the photoactivity of  $\text{TiO}_2$  is restricted to the UV region of the solar spectrum due to its large bandgap energy ( $\sim 3.2$  eV) (Mehta et al., 2016; Singh et al., 2016).  $\text{TiO}_2$  also suffers from accelerated recombination of the exciton species. Creating a heterojunction with a low bandgap semiconductor is one of the prevalent techniques to enhance its activity in the visible region and increase the charge separation (Coto et al., 2017). Layered two-dimensional transition metal dichalcogenides (2D-TMDs), such as molybdenum disulfide ( $\text{MoS}_2$ ) are promising candidate to designing a heterojunction catalyst alongside  $\text{TiO}_2$ .  $\text{MoS}_2$  has a layer depended band gap, for bulk the value is 1.2 eV and increases to 1.9 eV for monolayer (Liu et al., 2015a). Significant research work already reported on 2D- $\text{MoS}_2/\text{TiO}_2$  composites in photocatalytic dye pollutant removal process and hydrogen evolution owing to their favourable band alignments (Zhou et al., 2013a; He et al., 2016), where the conduction band edge of  $\text{MoS}_2$  nanosheets higher than that of  $\text{TiO}_2$  forms a type-II band alignment at  $\text{MoS}_2/\text{TiO}_2$  interfaces. It enhances the charge transfer rate and reduces the charge recombination rate (Ho et al., 2004; Xiang et al., 2012). The efficiency of  $\text{TiO}_2$ - $\text{MoS}_2$  composites to photo-degrade dye molecules is also depending on the number of layers in  $\text{MoS}_2$ , and the weight percentage of  $\text{MoS}_2$  loaded on  $\text{TiO}_2$  (Zhou et al., 2013b; Mehta et al., 2018). In these works,  $\text{MoS}_2$  explored as a light-driven catalyst and its dye removal

performance rely on crystalline phase (2H/1T), and surface charge potential. It is to be noted, that in most instances degradation capabilities of the photocatalyst is measure with regards to a individual dye solutions. However in real world scenarios the effluents consists of a plethora dyes mixed in unknown quantities. To the best of our knowledge, no work has been done to address the challenges in degrading mixed dye effluents.

In addition to being a semiconduction photocatalysts, MoS<sub>2</sub> has excellent adsorption properties as well (Li et al., 2019). The adsorption capability of 2D-MoS<sub>2</sub> is superior to its light-driven catalytic property and is relatively unexplored. The extended 2-D MoS<sub>2</sub> lattice diameter anticipated to percolate more pollutant quantity per hr compared to its photocatalytic process. Xin Xiao et al. synthesized MoS<sub>2</sub> nanoflower by hydrothermal method and explored the adsorption activity of 3-D structured MoS<sub>2</sub> towards cationic form Rhodamine B (RhB) dye molecules. The synthesized nanoflower MoS<sub>2</sub> showed high-level adsorption towards RhB (365 mg/g) in an acidic solution rather than an alkaline (Xiao et al., 2020). The dye adsorption level of MoS<sub>2</sub> can be increased if 2-D nanosheets/nanoflakes are prevented from aggregation to form 3-D microstructure MoS<sub>2</sub>, which increases specific surface area and adsorption sites. MoS<sub>2</sub> show more adsorption efficacy towards cationic dyes than anionic dyes due to the surface charge potential of MoS<sub>2</sub> (Han et al., 2017).

To enhance the adsorption activity of MoS<sub>2</sub> towards anionic dyes, Huan Yang et al. synthesized mesoporous C/MoS<sub>2</sub> composite by hydrothermal method. Introducing carbon into 2-D MoS<sub>2</sub> nanosheets reduced the degree of stacking in MoS<sub>2</sub> nanosheets and increased the surface area. Carbon in C/MoS<sub>2</sub> might have modified the surface charge potential of MoS<sub>2</sub> to enhance the adsorption of anionic dyes like Methyl orange (450mg/g) (Yang et al., 2020). It shows the flexibility involved in modifying the ionic property of MoS<sub>2</sub> by assembling other materials in-order to remove cationic or anionic dyes. Though the zwitterionic NF membranes remove both anionic and cationic charged pollutants, the removal efficiency is not identical for

anionic and cationic particles. Also, trace level dye molecules usually escape from the NF process, which should be treated with an appropriate secondary process like photoreforming or photocatalysis technique before channelizing the pollutants into the water bodies. In this line, the inclusion of sunlight driven photocatalyst in associate with adsorbent could reduce toxicity risk in the environment. Previous reports on hybrid adsorbent-photocatalyst approach result in excellent removal of diverse pollutants such as chemical (Vimonses et al., 2010), pharmaceutical drug (Długosz et al., 2015; Fanourakis et al., 2020), dye (Mohammadreza Miraboutalebi et al., 2020) and heavy metals (Kanakaraju et al., 2017) from water, but yet there is no demonstration for mixed dye pollutants removal using hybrid adsorbent-photocatalyst process. Also, the underlying mechanism of pollutant removal at hybrid adsorbent-photocatalyst surface is not well studied.

In this work, we report the harness the property of 2-D MoS<sub>2</sub> as an adsorbent in MoS<sub>2</sub>/TiO<sub>2</sub> nanocomposite where the widened lattice plays a critical role in determining the properties. Unlike conventional single-stage dye removal process, we propose a two-stage integrated adsorption and photocatalysis process to remove both anionic and catalytic dyes pollutants simultaneously. Briefly, in a stage-I significant fraction of dyes extracted at dark mode adsorption on ultrathin MoS<sub>2</sub> layers, and in stage-II, the dyes which are not adsorbed are degraded through the photocatalytic effect of TiO<sub>2</sub>. A mechanism is also proposed for these characteristics.

## **Experimental Section:**

### **Materials**

MPT-20 Titania paste (TiO<sub>2</sub>, anatase phase) having an average particle size of 20nm (Greatcell solar materials, Australia). Sodium molybdate dihydrate (Na<sub>2</sub>MoO<sub>4</sub>·2H<sub>2</sub>O, 99.5%), Thiourea (NH<sub>2</sub>CSNH<sub>2</sub>, 99%), Ethanol absolute, Methylene Blue (MB), Crystal Violet (CV), Rhodamine

B (RhB) and Methyl Orange (MO) were purchased from Sigma-Aldrich. All chemicals were used without further purification. Distilled water was used to prepare solutions of sodium molybdate and thiourea.

### **Synthesis of MoS<sub>2</sub> nanoflakes in 3D flower structure**

The MoS<sub>2</sub> was synthesized by using a simple hydrothermal method ((Raja et al., 2015; Mehta et al., 2018). Sodium molybdate dihydrate (0.5g) and thiourea (0.8g) are dissolved in 30 ml of distilled water (DI), and the solution volume was increased to 60 ml by adding 30 ml DI water, before transferring it to the Teflon lined stainless steel autoclave vessel (100ml volume). The hydrothermal treatment was carried out at 210 °C for 24 h and the system was naturally cooled. The obtained product was washed with ethanol and water, three times, respectively. The washed product was dried at 60 °C for 16 h and then mechanically ground to get fine powder particles.

### **Preparation of TiO<sub>2</sub> nanopowder solution**

MPT-20 Titania paste 10g was dispersed in 30 ml of ethanol and stirred for one hour to form a homogenous solution (solution A). The volume of the solution was increased to 60 ml by adding DI water and then transferred to the autoclave vessel. The other treatment and washing cycles were the same as the MoS<sub>2</sub> synthesis process.

### **Synthesis of MoS<sub>2</sub>/ TiO<sub>2</sub> nanocomposites**

The MoS<sub>2</sub>/TiO<sub>2</sub> nanocomposites with different weight % of MoS<sub>2</sub> (such as 2.5, 5, 10, 20, 30, and 50 wt%) were synthesized by the hydrothermal method. These nanocomposites are coined as TM 2.5%, TM 5%, TM 10%, TM 20%, TM 30% and TM 50%, respectively. Sodium molybdate and thiourea weight was varied in 30 ml DI water to form a homogenous aqueous solution. This solution was added dropwise to the TiO<sub>2</sub> solution (solution A), which forms a 60 ml solution volume, and the final solution was stirred for one hour. The hydrothermal

treatment condition was maintained the same as the synthesis of MoS<sub>2</sub> and TiO<sub>2</sub>. All powder samples, including MoS<sub>2</sub>, TiO<sub>2</sub>, and MoS<sub>2</sub>/TiO<sub>2</sub> nanocomposites, were annealed 150 °C for one hour under preheated atmospheric conditions.

## **Characterization**

The morphology of the samples was studied by high-resolution transmission electron microscopy (HRTEM, M/s. JEOL JEM 2100) and scanning electron microscopy (SEM, M/s/ ZEISS Supra 55VP). HRTEM was operated at 200 kV, and an SEM scan was done under InLens mode at 3 kV accelerating voltage. The electron microscopy images are analyzed using Digital Micrograph and ImageJ software tools. Crystalline property of the samples was investigated using X-Ray diffraction (XRD) and Raman spectroscopy. X-ray diffraction (XRD, M/s. BRUKER D8 Advance) pattern for all samples was recorded in the 2 $\theta$  range of 20-80° using Cu-K $\alpha$  radiation ( $\lambda = 0.154060$  nm) with a scan rate of 0.5° min<sup>-1</sup> at 40 kV and 40 mA. Raman spectra were obtained by using a Raman spectrometer (M/s. Horiba Jobin-Yvon LabRAM HR Evolution) with 514.5nm argon-ion LASER. The surface chemical state of samples was investigated by X-ray photoelectron spectroscopy (XPS, M/s. Kratos XSAM800) using non-monochromatic Mg K $\alpha$  (1253.6 eV) source. The sample spectra were analyzed using the CasaXPS software, and the peak shift due to any apparent charging was calibrated with respect to adventitious carbon C1s peak at 284.8 eV (reference). All the core level line shapes were background-subtracted with Shirley background, and peak fitting carried out with Gaussian (50%) and Lorentzian (50%) functions. Zeta potential measurement (ZP, M/s. ANALYTIK, Stabino) of the photocatalyst and the organic dyes were measured using oscillating piston design.

## **Adsorption and photocatalytic experiments**

The adsorption performance of all the samples at both cationic (MB, CV) and anionic (RhB, MO) dyes were analyzed. Under the dark condition, the powder sample (25 mg) were dispersed in the glass vessel containing 50 mL of dye solution (25mg/L of dye in 50 mL deionized water). The obtained solution was magnetically stirred (120 RPM) for 30 minutes under dark at room temperature to attain the adsorption/desorption equilibrium. The photocatalytic activity of the sample, the light source (Asahi Spectra HAL 320, 300 W, 75mW/cm<sup>2</sup>, 350-1100nm, AM1.5G filter) illuminated from the top with a distance of 30 cm from the liquid surface. The intensity of the light source was tuned to 1 SUN condition, with the light illuminated area of 50mm × 50mm. During the experiment cycle, 1mL aliquot of the dye solution was collected at a time interval of 30 mins. The liquid samples were centrifuged (1200 rpm, 10 minutes) and then transferred into a quartz cuvette (M/s. Hellma) to record the absorption spectra (250nm – 750nm) by using a UV-vis spectrophotometer (M/s. Thermo Scientific, Evolution 220). The experiment was repeated for the mixed dye solution (both anionic and cationic) having different concentrations (25mg/L and 50mg/L).

## Results and discussion

The XRD patterns of as-prepared TiO<sub>2</sub>, MoS<sub>2</sub> and MoS<sub>2</sub>/TiO<sub>2</sub> nanocomposites (TM 2.5%, TM 5%, TM 10%, TM 20%, TM 30% and TM 50%) were shown in **Figure 1**. The diffraction peaks of pure TiO<sub>2</sub> can be assigned to the (101), (103), (004), (200), (105), (211), (213), and (204) planes match the standard peak of anatase phase (Yang and Zeng, 2004; Perera et al., 2012; Dhandayuthapani et al., 2018). For pristine MoS<sub>2</sub>, the detected peaks are assigned to the (002), (100), (103), and (110) planes of the hexagonal phase (He et al., 2016). It is difficult to observe MoS<sub>2</sub> reflections in the MoS<sub>2</sub>/TiO<sub>2</sub> nanocomposites because MoS<sub>2</sub> is too thin to detect. (Chang and Chen, 2011; Lin et al., 2019).

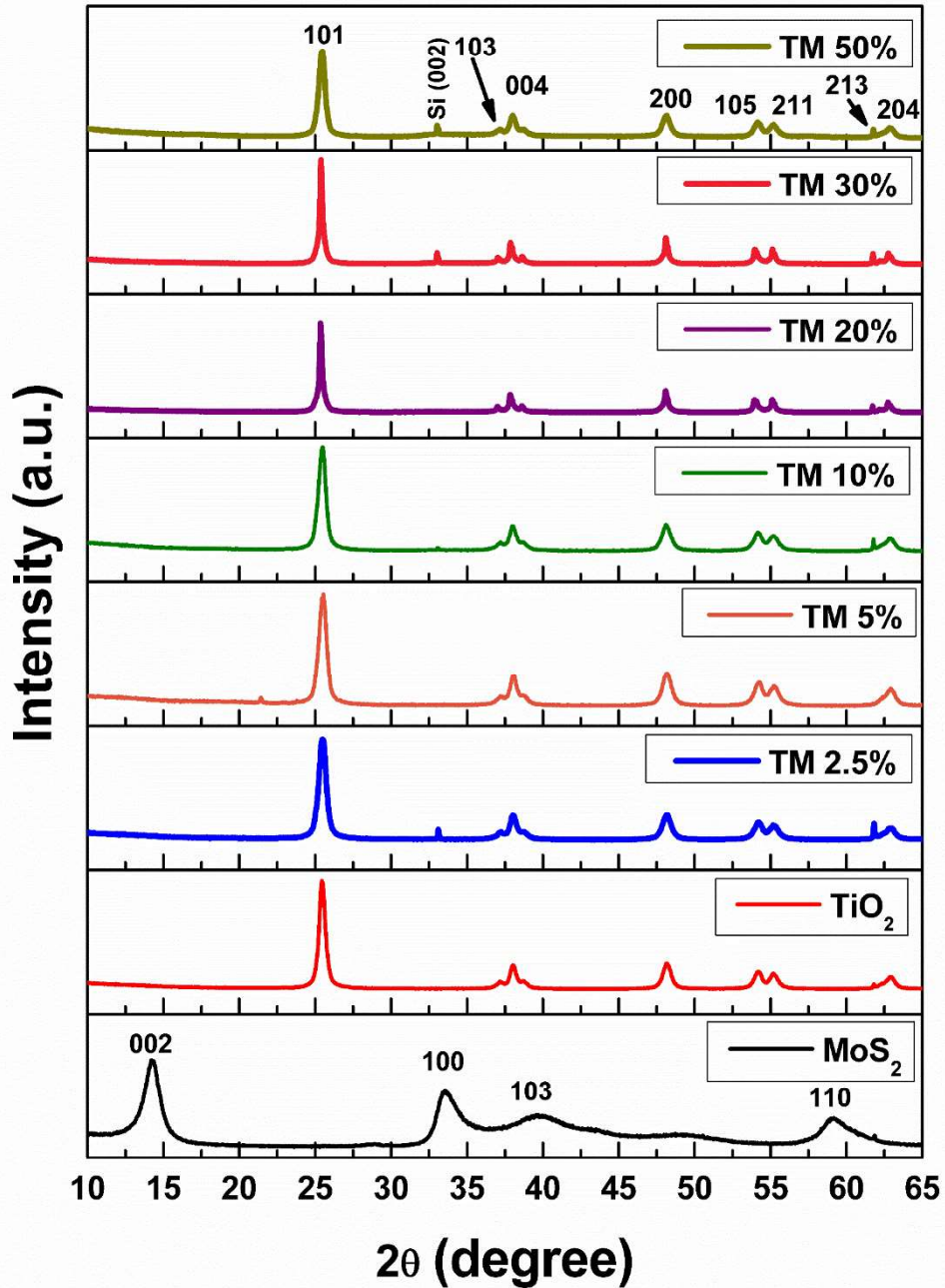


**Figure 1.** XRD pattern of pure MoS<sub>2</sub>, pure TiO<sub>2</sub>, and MoS<sub>2</sub>/TiO<sub>2</sub> composites with a different weight percentage of MoS<sub>2</sub>.

The SEM image of hydrothermal synthesized MoS<sub>2</sub> powder is presented in **Figure 2 (a)**. It shows a 3-D flower structure in 2 to 3-micron size. HRTEM in **Figure 2 (b) and (c)**, indicates few-layer 2-D nanoflakes were bundled together to form a 3-D flower structure. The interspace distance of crystal lattice is estimated from the HRTEM image (**Figure 2 (d) and**

(e)) and found to be 0.64 nm. This is corresponding to the (002) crystalline phase of MoS<sub>2</sub>. In the case of 10 wt %, MoS<sub>2</sub> coated TiO<sub>2</sub> (TM 10%), the aggregated nanoflakes presence in the pristine MoS<sub>2</sub> became debundled by few-layer sheets (**Figure 2 (f)**). These debundled few-layer MoS<sub>2</sub> nanosheets are coated on the TiO<sub>2</sub> surface, due to high van der Waal force during hydrothermal synthesis (Wu et al., 2019) (Duong et al., 2017) where the TiO<sub>2</sub> nanoparticles act as a substrate for the growth of a few-layered 2-D MoS<sub>2</sub> nanoflake. It was difficult to differentiate the TiO<sub>2</sub> nanoparticles and MoS<sub>2</sub> nanoflakes from SEM images (**Figure S1**). But, the HRTEM image (**Figure 2 (g)**) of TM10% illustrated a well-defined grain boundary between the MoS<sub>2</sub> (002) phase and the TiO<sub>2</sub> (101) phase, which indicates the MoS<sub>2</sub>/TiO<sub>2</sub> heterostructures. Interestingly, the diameter of the MoS<sub>2</sub> interspace layer is increased to 0.88 nm (**Figure 2 (g) and (h)**) at MoS<sub>2</sub>/TiO<sub>2</sub> compared to pristine MoS<sub>2</sub> (0.64 nm) in **Figure 2 (d) and (e)**. The widening/expanding in the interlayer spacing of MoS<sub>2</sub> can be explained by the solvent effect. The ethanol is used as co-solvent in MoS<sub>2</sub>/TiO<sub>2</sub> in hydrothermal reaction, resulting in increasing the interspace layer of MoS<sub>2</sub>. In the hydrothermal process, Mo and S ions react to form MoS<sub>2</sub> nucleus, the resultant MoS<sub>2</sub> nucleus further accumulates and then grow into layered nanosheets through a ripening process (Xu et al., 2017). Here, the ethanol molecules gets trapped between the layers of MoS<sub>2</sub>, which weakens the van der Waals force and widens the interspace distance (Qi et al., 2015; Tao et al., 2020).

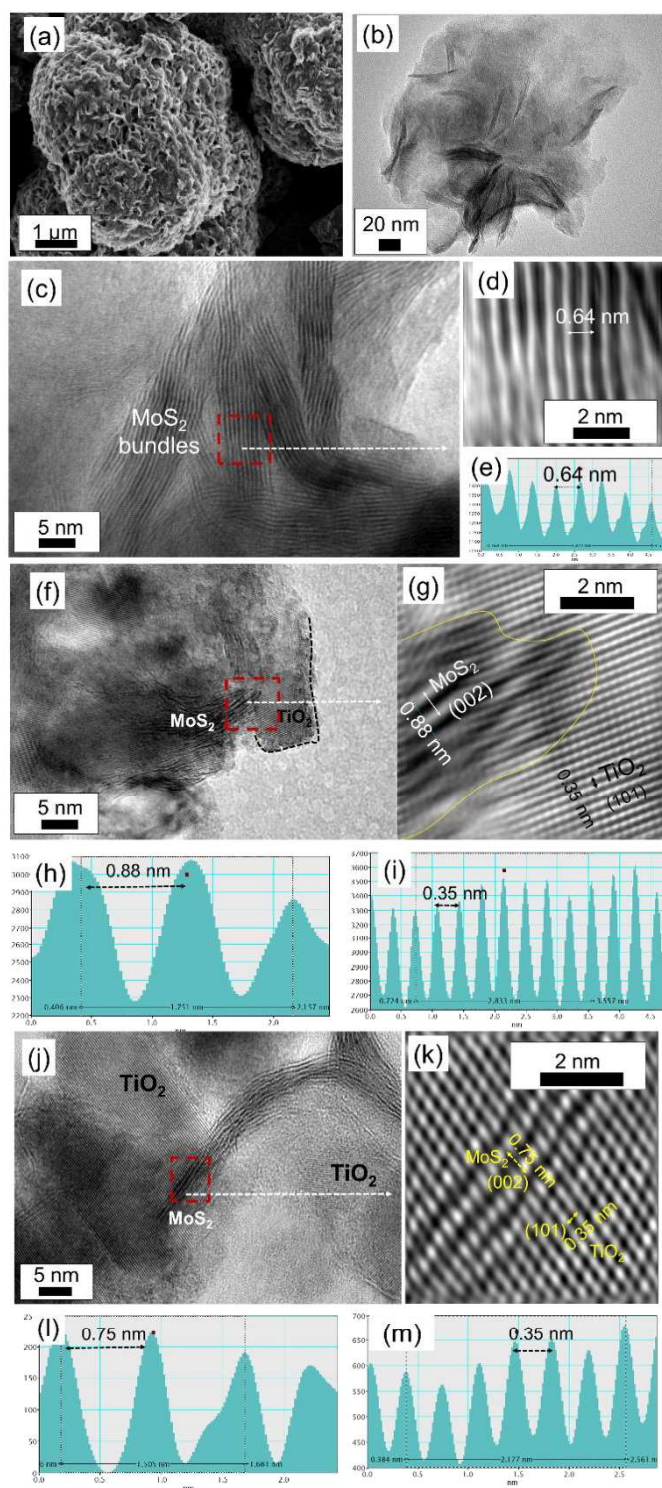


**Figure 2.** (a) SEM image of MoS<sub>2</sub>. HRTEM images of MoS<sub>2</sub> measured at (b) 20 nm scale and (c) 5 nm scale. (d) High magnification TEM image of interlayers seen in Figure 2(c) at 2nm scale, and (e) respective inverse FFT image of MoS<sub>2</sub> interlayers. (f) HRTEM image of TM 10% (TiO<sub>2</sub>/MoS<sub>2</sub>) composite, (g) High magnification TEM image of interlayers seen at Figure 2(f) at 2nm scale, and Inverse FFT images of (h) MoS<sub>2</sub> interlayers (i) TiO<sub>2</sub> interlayers marked in Figure 2(g). (j) HRTEM image of TM 50% (TiO<sub>2</sub>/MoS<sub>2</sub>) composite, (k) High magnification TEM image of interlayers seen at Figure 2(j) at 2nm scale, and Inverse FFT images of (l) MoS<sub>2</sub> interlayers (m) TiO<sub>2</sub> interlayers marked in Figure 2(k).

Also, at high temperature, weakened S-S van der Waals interactions reduces the restacking probability of MoS<sub>2</sub> (Geng et al., 2016; Alomar et al., 2019) may also be responsible for widening the interspace layer. Further increasing the ratio of MoS<sub>2</sub> at composite TM 50% the interspace distance of MoS<sub>2</sub> is increased to 0.75 nm (**Figure 2 (j-l)**) but this increase is lesser than TM 10%. The widening of MoS<sub>2</sub> interspace layer implies the transformation of 2H crystal phase towards 1T phase, resulting in partial phase conversion of MoS<sub>2</sub> in nanocomposites. (Tao et al., 2020) Higher the wt% of MoS<sub>2</sub> lead to the increase in layer stacking and reduces the interspace distance of MoS<sub>2</sub>. However, the interspace distance of TiO<sub>2</sub> remains constant in both TM 10% (**Figure 2 (i)**) and TM 50% samples (**Figure 2(m)**) due to its thermal stability.

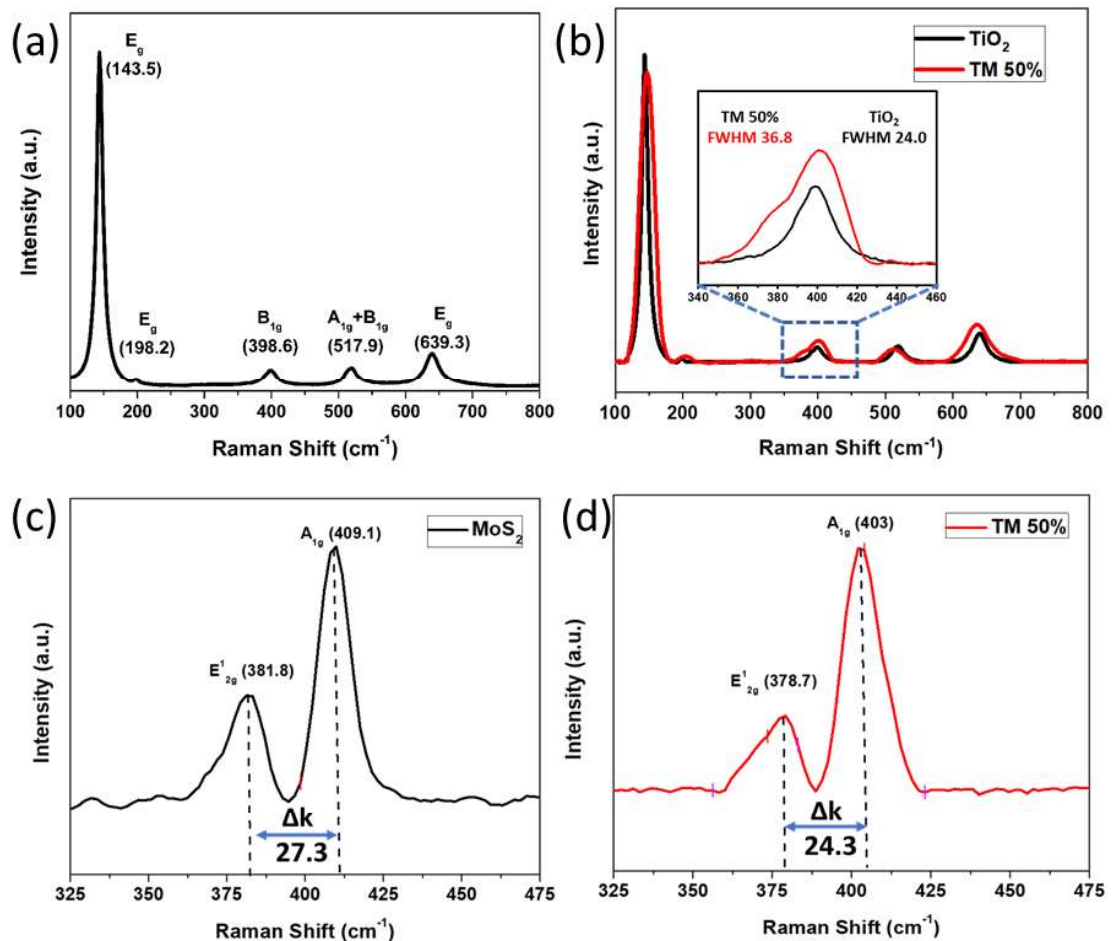


**Figure 3.** (a) Raman spectrum of TiO<sub>2</sub> showing active modes of anatase phase, (b) Raman spectra comparison of TiO<sub>2</sub> and TM50% showing peak shift and peak broadening in the insert figure, (c)

Raman spectra of MoS<sub>2</sub> vibrational peaks ( $E_{2g}^1$  and  $A_{1g}$ ) in MoS<sub>2</sub> and (d) TM 50% (MoS<sub>2</sub>/TiO<sub>2</sub> composite).

Raman spectroscopy was carried out on the pristine MoS<sub>2</sub>, pristine TiO<sub>2</sub>, and TM 50% nanocomposite samples. In the spectrum obtained for TiO<sub>2</sub> (**Figure 3a**), the Raman active modes were observed at 143.5 cm<sup>-1</sup>(E<sub>g</sub>), 198.2 cm<sup>-1</sup>(E<sub>g</sub>), 398.6 cm<sup>-1</sup>(B<sub>1g</sub>), 517.9 cm<sup>-1</sup> ( $A_{1g}$  + B<sub>1g</sub>) and 639.3 cm<sup>-1</sup> (E<sub>g</sub>), which confirms the presence of anatase phase (Choi et al., 2005). The spectrum obtained for pristine MoS<sub>2</sub> (**Figure 3c**) shows two prominent peaks, which correspond to the in-plane vibration of Mo and S atoms ( $E_{2g}^1$  at 381.8 cm<sup>-1</sup>) and out-of-plane vibration of S atoms ( $A_{1g}$  at 409.1 cm<sup>-1</sup>). The Raman spectra obtained for TM 50% (**Figure 3b**), confirms the presence of TiO<sub>2</sub> anatase phase, by matching with Raman peak values of pristine TiO<sub>2</sub>. However, the MoS<sub>2</sub> peaks between the region 360 cm<sup>-1</sup> to 410 cm<sup>-1</sup> are superimposed by TiO<sub>2</sub> peak B<sub>1g</sub> (398.6 cm<sup>-1</sup>), which unveils peak broadening and could not differentiate MoS<sub>2</sub> and TiO<sub>2</sub> Raman active peaks. And thus, MoS<sub>2</sub> Raman spectrum acquired with a reduction in the acquisition rate for the nanocomposite TM 50%, and this condition was not favourable to acquire MoS<sub>2</sub> Raman peaks for the samples having less than 50wt% of MoS<sub>2</sub>. Kim et al reported that, lesser the frequency difference ( $\Delta k$ ) between  $E_{2g}^1$  and  $A_{1g}$  of MoS<sub>2</sub>, the lesser is the number of MoS<sub>2</sub> layers (Kim et al., 2016). The Raman spectrum obtained for TM 50% (**Figure 3d**) shows that the frequency difference ( $\Delta k$ ) reduced from 27.3 cm<sup>-1</sup> (MoS<sub>2</sub>) to 24.3 cm<sup>-1</sup> (nanocomposite), which suggests that the number of layers has been reduced from multilayer nanoflakes in pristine MoS<sub>2</sub> to few-layer nanoflakes in the TM 50% nanocomposite. This is in line with HRTEM results of 3-D flower structure (**Figure 2 (c)**) debundled to 2-D nanoflakes (**Figure 2 (f) and (j)**).

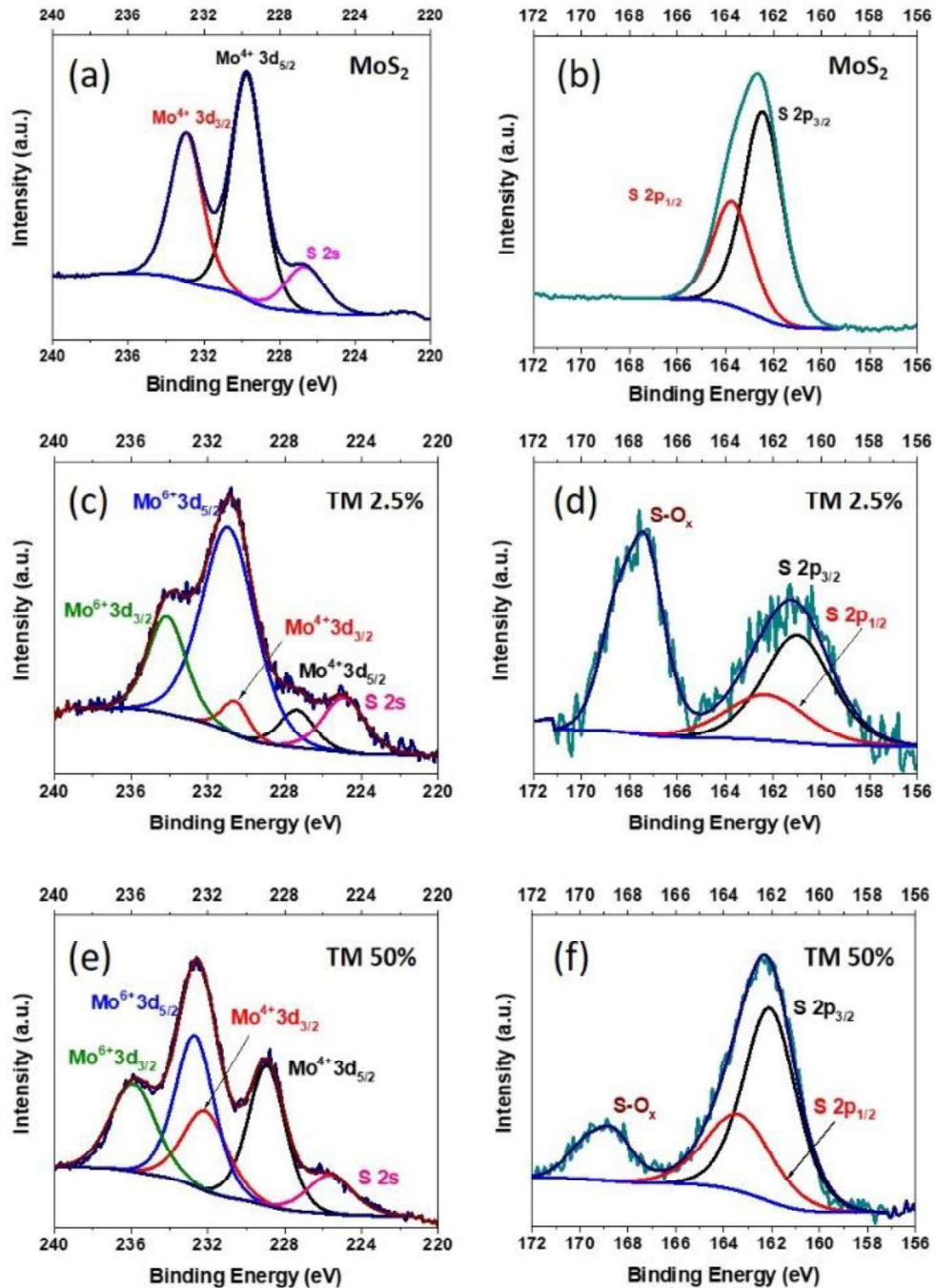


**Figure 4.** XPS core level spectra of Mo3d and S2p measured at (a) and (b) MoS<sub>2</sub>; (c) and (d) TM 2.5% (TiO<sub>2</sub>/MoS<sub>2</sub> composite) and; (e) and (f) TM 50% (TiO<sub>2</sub>/MoS<sub>2</sub> composite).

Herein, XPS is used to understand the charge state and chemical bonding information of these composites. In **Figure 4 (a)- (f)** MoS<sub>2</sub> and MoS<sub>2</sub>/TiO<sub>2</sub> nanocomposite (TM 2.5% and TM 50%) are presented. Irrespective of MoS<sub>2</sub> wt%, the analysis of deconvoluted Mo3d spectra (**Figure 4 (a), (c), and (e)**) in all nanocomposite samples shows two oxidation states of

Molybdenum,  $\text{Mo}^{4+}$  and  $\text{Mo}^{6+}$ . The  $\text{Mo}3d$  spectrum of TM 2.5% sample (**Figure 4 (c)**) shows peak at 227.36eV, 230.56eV, 230.92eV and 234.12eV can be ascribed to  $\text{Mo}^{4+} 3d_{5/2}$  ( $\text{MoS}_2$ ),  $\text{Mo}^{4+} 3d_{3/2}$  ( $\text{MoS}_2$ ),  $\text{Mo}^{6+} 3d_{5/2}$  ( $\text{MoSO}_4 / \text{MoO}_3$ ) and  $\text{Mo}^{6+} 3d_{3/2}$  ( $\text{MoSO}_4 / \text{MoO}_3$ ), respectively (Liu et al., 2019). The presence of sulfide ( $\text{MoS}_2$ ,  $\text{Mo}^{4+}$ ) and sulfate ( $\text{MoSO}_4$ ,  $\text{Mo}^{6+}$ ) also confirmed from the analysis of deconvoluted  $\text{S}2p$  spectra (**Figure 4 (b), (d) and (f)**) in all samples (Liu et al., 2015b) (Zhou et al., 2016). The  $\text{S}2p$  spectrum of TM 2.5% (**Figure 4 (d)**) shows two distinct peaks having binding energy (BE) position at 161.31eV and 167.45eV, which can be assigned to sulfides and sulfates, respectively. The sulphide peak is deconvoluted further which gave rise to two peaks at the BE position 160.99eV ( $\text{S}2p_{3/2}$  -  $\text{MoS}_2$ ) and 162.29 eV ( $\text{S}2p_{1/2}$  -  $\text{MoS}_2$ ) indicating 2H- $\text{MoS}_2$  (Vrubel et al., 2012). It also noted that by increase in  $\text{MoS}_2$  wt% in the  $\text{MoS}_2/\text{TiO}_2$  composites, there was increase in sulfide  $\text{Mo}^{4+}$  ( $\text{MoS}_2$ ) peak area and decrease  $\text{Mo}^{6+}$  sulfate ( $\text{MoSO}_4$ ) peak area. From the **Table S1**, it is shown that the peak positions of  $\text{Mo}3d$  and  $\text{S}2p$  shift towards higher BE level (i.e., shows redshift) with an increase in  $\text{MoS}_2$  wt% and pristine  $\text{MoS}_2$  shows higher BE. The decrease in BE shown in TM nanocomposites was might be due to the partial transition of 2H  $\text{MoS}_2$  to 1T  $\text{MoS}_2$  (Wang et al., 2017; Gan et al., 2018; Wang et al., 2018) and this phase conversion was also confirmed through the widening of  $\text{MoS}_2$  interspace layer through HRTEM. The oxidized S was revealed from the emission peaks at 167.45 eV (TM 2.5%) and 168.6 eV (TM 50%), which is relative to the partial oxidation of unsaturated S of the nanosized layers of  $\text{MoS}_2$ . The  $\text{Mo}3d$  spectrum of pristine  $\text{MoS}_2$  (**Figure 4 (a)**) shows two peaks at 229.73 eV and 232.93 eV, which originate from the doublets  $\text{Mo} 3d_{5/2}$  and  $\text{Mo} 3d_{3/2}$ . The  $\text{S}2p$  spectrum of pristine  $\text{MoS}_2$  (**Figure 4 (b)**) shows two peaks at 162.44 eV and 163.73 eV, corresponding to the  $\text{S} 2p_{3/2}$  and  $\text{S} 2p_{1/2}$  orbitals of the divalent sulfide ions ( $\text{S}^{2-}$ ). From the core-level spectra of pristine  $\text{MoS}_2$  ( $\text{Mo}3d$  and  $\text{S}2p$ ) it was confirmed the absence of sulfate group. The binding energies showed in **Table S1** are in good agreement with reported XPS results of  $\text{MoS}_2$ . (Weber et al., 1996; Li et al., 2017; Xi et

al., 2019) The formation of molybdenum sulfate ( $\text{MoSO}_4$ ) within  $\text{MoS}_2/\text{TiO}_2$  composites might be due to the presence of ethanol during the synthesis process. Ethanol was not used in pristine  $\text{MoS}_2$  synthesis, and thus, this justifies the absence of sulfate group in pristine  $\text{MoS}_2$ . The removal and photocatalytic degradation of dye pollutants by  $\text{MoS}_2$  and  $\text{MoS}_2/\text{TiO}_2$  samples were qualitatively studied using methylene blue (MB) (25 mg/L). At the first 30 minutes,  $\text{MoS}_2/\text{TiO}_2$  samples were kept at MB dye solution under the dark condition, to explore the capable of dye adsorption. Then light illumination was allowed in the photocatalytic reactor for a few hours and analyzed the photocatalytic degradation process. Briefly, change in dye concentration at dark conditions infers the physical removal of dye molecules from solution to the adsorbent surface. Under light illumination, the semiconductor produces photocharge carriers (photoelectron and photohole) at the conduction band and valence band, which generate superoxide and hydroxyl radicals, respectively. Briefly, the photogenerated holes and electrons react with water and dissolved oxygen to form hydroxyl radical ( $\cdot\text{OH}$ ) and superoxide radical ( $\cdot\text{O}_2^-$ ). These high energy species ( $\cdot\text{OH}$  and  $\cdot\text{O}_2^-$ ) undergo multiple reactions with the organic pollutants in the aqueous medium to degrade pollutants. (Han et al., 2018) **Figure 5 (a)** shows the percentage of the ratio between final dye concentration ( $C$ ) and initial ( $C_0$ ) vs. time. From **Figure 5 (a)**, in the absence of adsorbent or photocatalyst materials, only light illumination (photolysis) does not change in dye concentration. After introducing the  $\text{MoS}_2$ ,  $\text{TiO}_2$ , and  $\text{MoS}_2/\text{TiO}_2$  nanocomposite samples in the dye solution, a significant change in MB dye concentration has been noticed at dark and light illumination conditions. In particular, **Figure 5 (a)** shows two types of changing behaviour in  $(C/C_0)$  values. Under the dark condition, the  $\text{MoS}_2$ ,  $\text{TiO}_2$ , and TM 2.5% sampled showed less change in  $(C/C_0)$  value indicates poor dye adsorption on their surface. Under light illumination condition, the rate of change in  $(C/C_0)$  values are ordered as TM 2.5% > TM 5% > TM 10% > TM 20% > TM 30% > TM 50% >  $\text{TiO}_2$  >  $\text{MoS}_2$ .

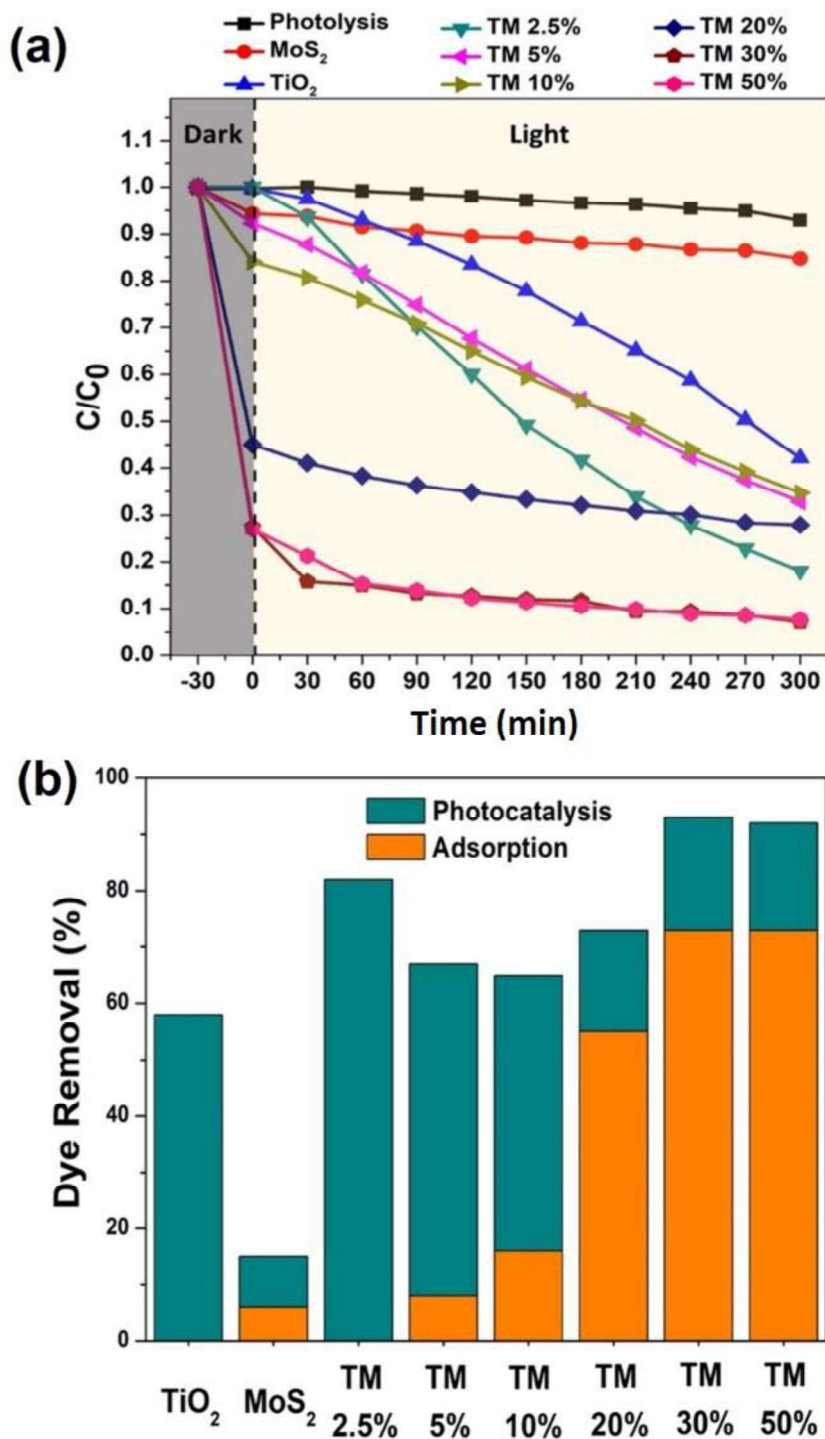


**Figure 5.** (a) Photocatalytic degradation, (b) dye removal efficiency of MB dye by  $\text{TiO}_2$ ,  $\text{MoS}_2$  and  $\text{MoS}_2/\text{TiO}_2$  nanocomposites with a different weight percentage of  $\text{MoS}_2$ . Note that the catalyst loading quantity is 25 mg in 50 ml dye solution.

The higher photocatalytic dye degradation rate observed at TM 2.5% nanocomposite might be due to effective charge separation at  $\text{MoS}_2/\text{TiO}_2$  heterointerfaces. This photoexcited charges (electrons and holes) further reacts with water molecules to produce superoxide and

hydroxyl radicals, which degrade the dye molecules. However, higher loading (above 2.5 wt %) of MoS<sub>2</sub> with the nanocomposite samples reduces the photocatalytic effect. The major plausible reason is the shielding effect of MoS<sub>2</sub>, which hinders the interaction of the dye pollutants with TiO<sub>2</sub>. This shows that in MoS<sub>2</sub>/TiO<sub>2</sub> composite, TiO<sub>2</sub> plays a predominant role as a photo-harvester, and MoS<sub>2</sub> act majorly as a co-catalyst to enhance the charge separation. (Zhou et al., 2016) Further analyzing the results in **Figure 5 (a)**, the C/C<sub>0</sub> values of TM 20%, TM 30%, and TM 50% showed effective dye adsorption in dark conditions. The adsorption of MB gets saturated beyond 30wt% of MoS<sub>2</sub> in composite samples and the highest adsorption efficiency of 73% of MB dye is noticed in TM 50 wt% sample. As observed in the HRTEM image, the interspace distance of MoS<sub>2</sub> lattice facilitates the penetration of dye molecules into the interior spaces of 2-D nanoflakes. Similarly, interspace mediated heavy metal (Hg and Pb) removal was demonstrated in 2-D MoS<sub>2</sub> adsorbents (Ai et al., 2016; Kumar et al., 2019). The major portion of remaining 27% of dye after adsorption on TM 50% samples are degraded by the photocatalysis process. Overall, TM 2.5% results in weak dye adsorption with high photocatalytic dye degradation, and TM 50% results in high dye adsorption with less photocatalytic activity. The dye removal (%) values of different materials were estimated from **Figure 5(a)** and summarised in **Figure 5 (b)**. **Figure 5 (b)** illustrates any material such as pristine MoS<sub>2</sub>, TiO<sub>2</sub>, or MoS<sub>2</sub>/TiO<sub>2</sub> composites couldn't remove the dye completely, either dark or light illumination condition. It requires combinatorial action of adsorption and photocatalytic degradation for complete dye removal. However, the complete dye removal process took over around 5hr. From an industrial viewpoint, the water treatment process time is a crucial factor that decides the effective cost involved with treatment.

It is worth to compare the TiO<sub>2</sub>/MoS<sub>2</sub> composite to carbon-TiO<sub>2</sub> composite as many researchers previously demonstrated it for hybrid adsorption/photocatalysis system. Though carbon-TiO<sub>2</sub> composite represents the adsorption-photocatalysis model, the light-blocking

effect by carbon to TiO<sub>2</sub> and surface area reduction by TiO<sub>2</sub> to carbon is a significant challenge in this system. Moreover, carbon does not contribute to light absorption to TiO<sub>2</sub>. In the 2-D MoS<sub>2</sub>, it has considerable light absorption behaviour, which is beneficial to TiO<sub>2</sub> (**Figure S3**). Unlike carbon particles, a thin few-layered 2D sheet does not block the light to TiO<sub>2</sub> as it is transparent in the UV wavelength region. It supports the photocatalytic activity of TiO<sub>2</sub>. The type-II energetic formation at TiO<sub>2</sub>/MoS<sub>2</sub> interfaces facilitates the photo charge carrier transfer from TiO<sub>2</sub> to pollutants, promoting the pollutants removal rate. One can question the materials synthesis cost of carbon-TiO<sub>2</sub> may not be comparable to TiO<sub>2</sub>/MoS<sub>2</sub>. But continuous research in this field will pave pathways to large-scale production, which might reduce the materials cost.

To reduce the time duration for the complete removal of dye molecules, we propose two-stage water treatment utilizing the different functional properties of MoS<sub>2</sub>/TiO<sub>2</sub> composites instead of a single material. **Figure 6** illustrates the schematic of two-stage dye pollutant removal/degradation. The high adsorption behaviour of TM 50% helps to remove the dye quickly, and the remaining dye molecules will be degraded by TM 2.5% photocatalyst. Therefore, involving TM 50% at stage-I and TM 2.5% at stage-II could remove the dye pollutant in a short span of time.

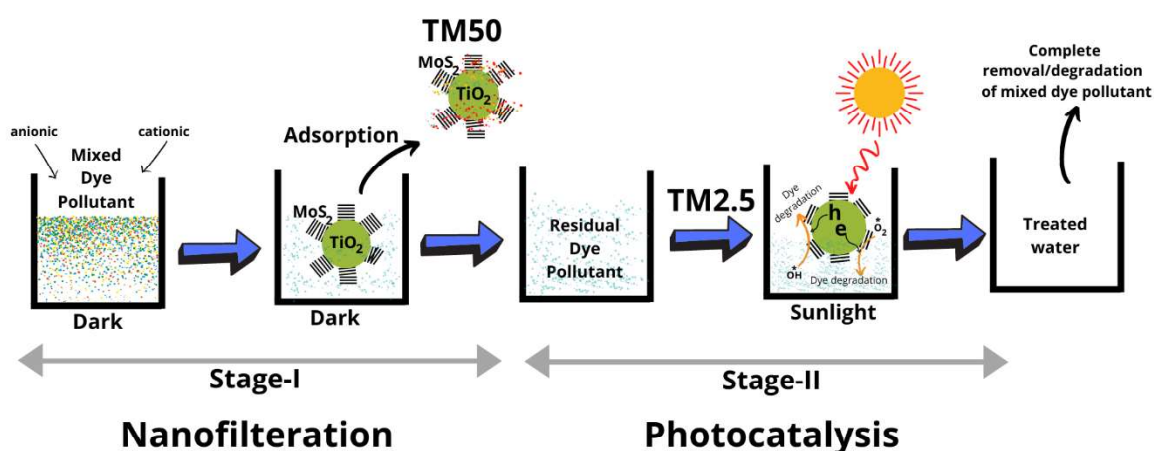


**Figure 6.** Schematic illustration of two-stage rapid-adsorption and photocatalysis based dye pollutant removal.

Two-stage based dye degradation rate vs. time plot for MB dye pollutants are presented in **Figure 7(a)**. The percentage of dye removal is estimated from **Figure 7 (a)** and summarised in **Figure 7 (b)**. From **Figure 7 (a)** and **7 (b)**, a complete 100% of MB dye degradation was achieved within 1hr. It demonstrate that a two-stage adsorption/photocatalysis integrated approach is highly effective in reducing the treatment time from 5hr to 1hr compared to a single material-based dye degradation process. The same procedure has been followed for other dyes like CV, RhB and MO. TM 50% showed very strong adsorption property towards cationic dyes (CV and MB) compared to anionic dyes (RhB and MO). This can be ascribed to the electrostatic interaction between the samples and dyes.

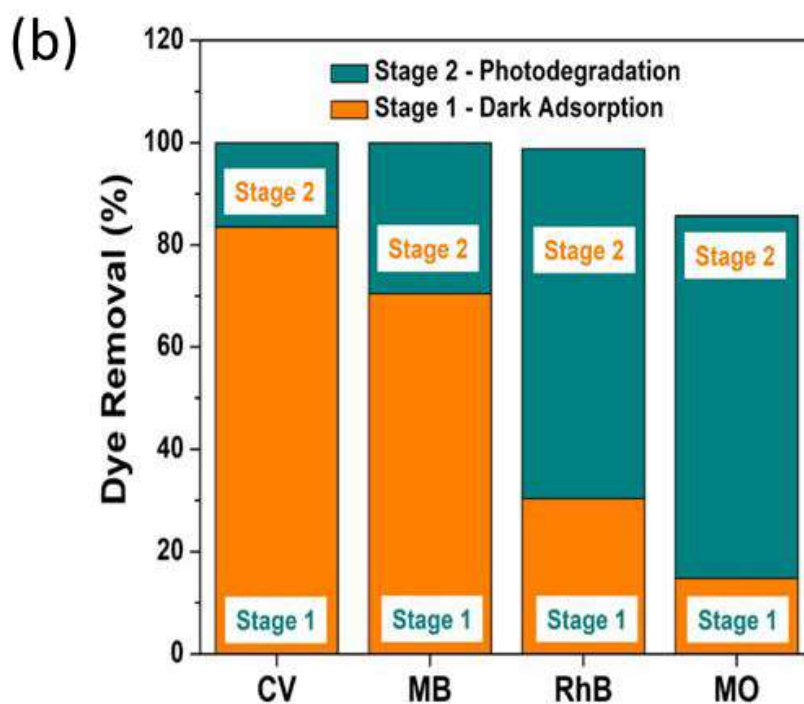
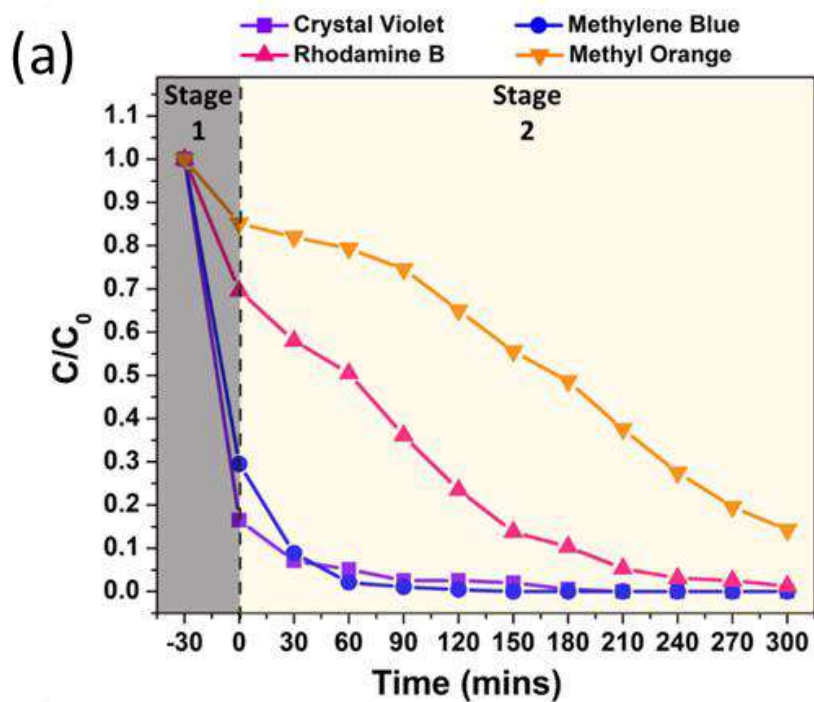


**Figure 7.** (a) Dark adsorption (stage 1) at TM50%, and photocatalytic degradation (stage 2) at TM2.5% samples. (b) Dye removal efficiency of MB, MO, RhB and CV dyes estimated from Figure 7 (a).

To decipher the inter-relationship between the surface charge of the MoS<sub>2</sub> adsorbent and dye molecules, we examine the Zeta potential (ZP) value of the MoS<sub>2</sub>, TiO<sub>2</sub>, and MoS<sub>2</sub>/TiO<sub>2</sub> nanocomposite samples (**Figure 8 (a)**). From **Figure 8 (a)**, it clearly understands

that MoS<sub>2</sub>/TiO<sub>2</sub> samples shifts towards negative potential with an increase in MoS<sub>2</sub> wt%. Increase in MoS<sub>2</sub> wt% increases the acidic nature of the samples by lowering the pH from 4.08 (TM 2.5%) to 3.3 (TM 50%).

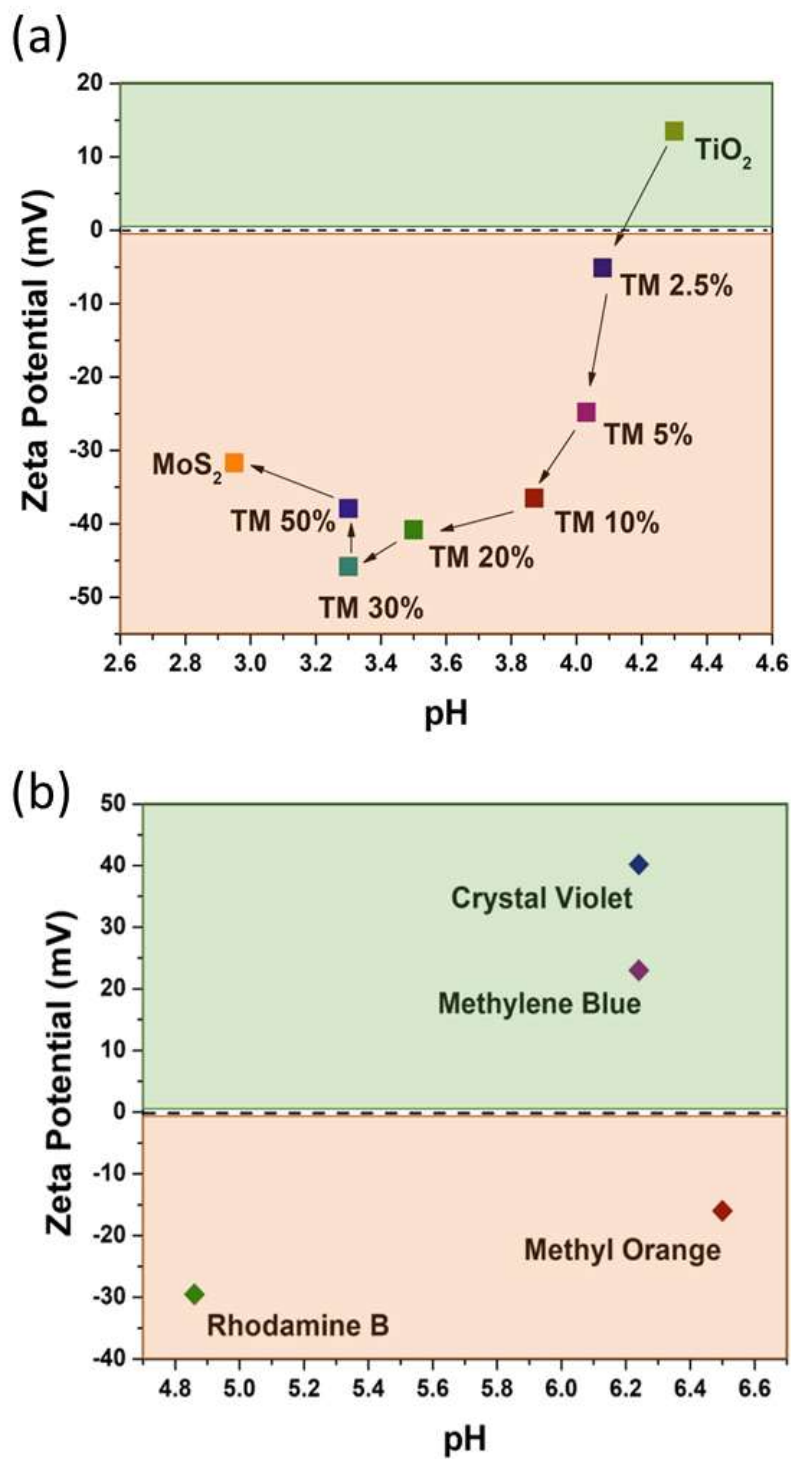


**Figure 8.** (a) pH vs Zeta Potential of pristine TiO<sub>2</sub>, MoS<sub>2</sub> and TiO<sub>2</sub>/MoS<sub>2</sub> composites (TM 2.5%, TM 5%, TM 10%, TM 50%), pH vs Zeta Potential of MB, CV, RhB and MO dyes.

Though TM 30% showed higher negative potential (-45.8 mV) than TM 50% (-37.9 mV), they both showed the same adsorption efficiency (73%) and pH value (3.3). Due to high negative potential value and an increase in surface area compared to MoS<sub>2</sub>, TM 50% showed greater affinity towards cationic dyes like CV (+40.2 mV) and MB (+23 mV). Though RhB was reported as a cationic dye (Chin et al., 2018), the ZP measurement showed it to be anionic (**Figure 8b**), and RhB (-29.5 mV) showed more negative potential than MO (-16 mV). For ZP value, the negative potential TM 50% should exhibit less adsorption towards RhB compared to MO. But in contrast, TM 50% showed less adsorption activity towards MO rather than RhB. Generally, anionic dyes show an increase in adsorption under low pH conditions (Salleh et al., 2011) and because of this condition, RhB (4.86 pH) showed a higher level of adsorption compared to MO (6.5 pH). Since TiO<sub>2</sub> showed no adsorption of dyes (cationic/anionic), and this confirms that the adsorption of dyes molecules is only due to the presence of MoS<sub>2</sub> within the nanocomposites.

We further validate the two-stage dye pollutant treatment in mixed dye solution with two different dye concentration. Anionic (RhB and MO) and cationic (MB and CV) dye solutions are mixed to attain 25mg/L and 50mg/L of 50ml mixed dye solution volume. The optical absorbance spectrum of mixed dye solution (**Figure S2**) was obtained showing the approximate spectra region of individual dyes. As is expected TM 50% (**Figure 9a**) removed 100% of cationic dyes and 70% of anionic dyes from the mixed dye solution having a concentration of 25mg/L under stage I - dark mode adsorption. This explains that 2D- MoS<sub>2</sub> having a high affinity towards cationic dye. The remaining 30% of anionic dyes are degraded in stage II - light mode (**Figure 9b**) i.e, the photocatalytic process completely degrading 30% of anionic dye after 3.5h. To understand the saturation level of cationic dyes adsorption onto TM50% surface at stage I, the dye concentration of mixed dye solution is doubled to have the

dye concentration 50mg/L. After increasing the concentration of mixed dye from 25 to 50mg/L, **Figure 9c** showed that 86% of cationic dyes and just 36% of anionic dyes were removed.

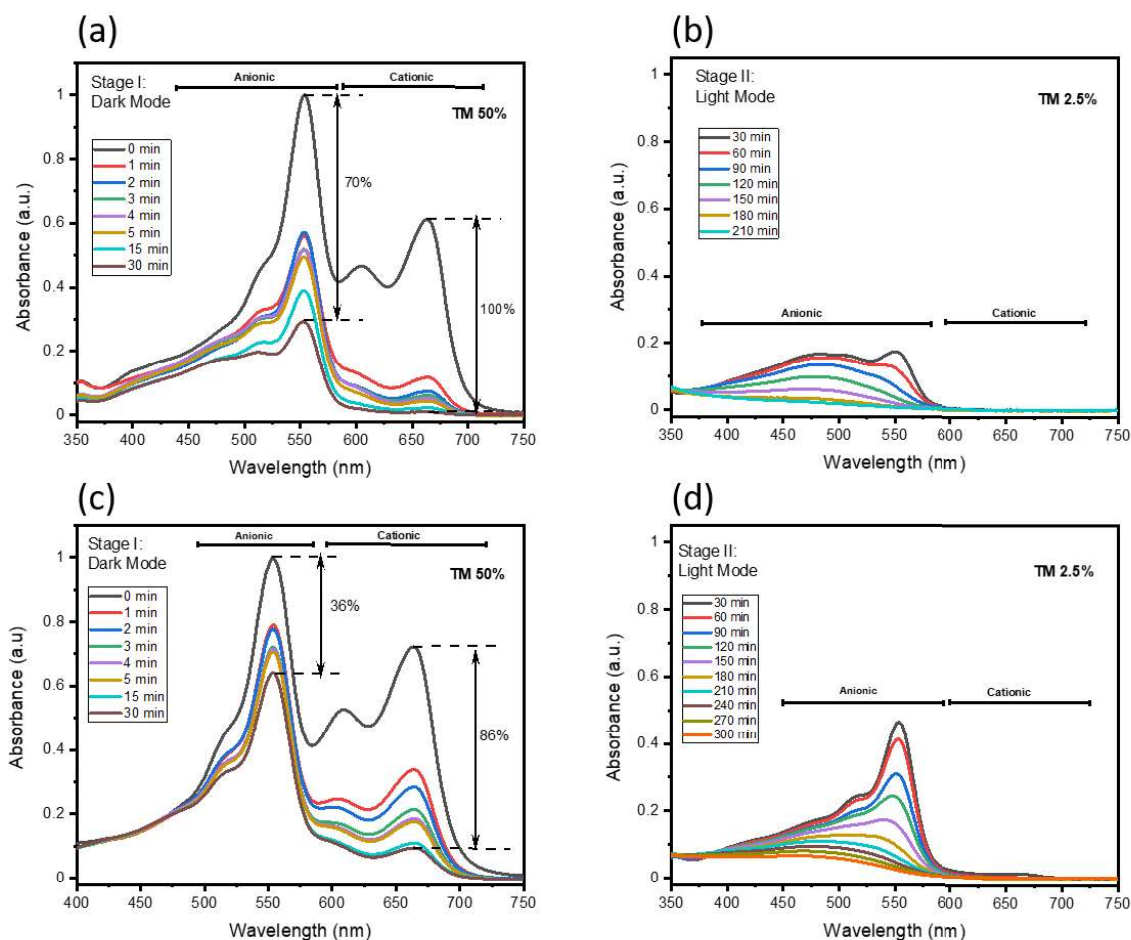


**Figure 9.** Optical absorbance spectra of mixed dye (anionic and cationic dye - 25mg/l) for a different period (a) after stage I treatment under dark mode using TM50%. (b) after stage II treatment under light irradiation condition using TM2.5%. Optical absorbance spectra of mixed dye (anionic and cationic dye - 50mg/l) for a different period (c) after stage I treatment under dark mode using TM50%. (d) after stage II treatment under light irradiation condition using TM2.5%.

It implies that dye adsorption at stage-I relies on the surface area of the TM50%. The remaining 14% of cationic dyes and 64% of anionic dyes are further degraded in stage II- light mode (**Figure 9d**) photocatalytic degradation stage which took about 5h. Qualitatively, the adsorption of dye molecules towards the TM50% is a rapid process in which more than 60% of dye molecule adsorption occurs in a minute (**Figure 9** and **Figure S4**). The dye adsorption

activity for 50mg/L dye concentration solution gets saturated in 15 minutes, whereas in 25mg/L the adsorption activity was active throughout 30 minutes under dark mode stage. This might be due to the trade-off between the surface area of TM50% and dye molecules concentration can be overwhelmed by enhancing the quantity of TM50% in the reactor. The above results evident that two-stage dye pollutant removal process using TM50% and TM2.5% be an effective route for tackling both single as well as mixed dye compounds in the textile waste. The stability of the benchmarking photocatalyst sample TM2.5% has been tested for 3 consecutive cycles (**Figure S5**). Photocatalytic degradation performance is almost sustainable even at third cycle implies the stability of the TM2.5%. It is worthy to implement this approach in real-time pre-treated textile dye pollutant where classical photocatalysis or filtration approach not able to resolve it completely.

## **Conclusions**

Ultrathin, few-layered 2-D MoS<sub>2</sub> mediated adsorption sites are created onto light active TiO<sub>2</sub> host nanoparticles by a single-step hydrothermal process. The TiO<sub>2</sub> host nanoparticles served dual role in protecting 2-D MoS<sub>2</sub> nanoflakes from undesired aggregation and widen interlayer spacing of MoS<sub>2</sub> sheet which favourable for accessing interior surface of MoS<sub>2</sub> in effective dye-adsorption compared to pristine 3-D MoS<sub>2</sub> structure. Nanocomposites with high MoS<sub>2</sub> wt% (TM 50%) and low MoS<sub>2</sub> wt% (TM 2.5%) showed high adsorption, and photocatalytic activity towards cationic and anionic dyes, respectively. Two-stage integrated adsorption and photodegradation dye removal process was evaluated using MoS<sub>2</sub>/TiO<sub>2</sub> nanocomposites. For the first time, a mixed dye (anionic and cationic) pollutant model was demonstrated as a proof-of-concept towards textile wastewater treatment. The ultrathin MoS<sub>2</sub>/TiO<sub>2</sub> nanocomposite developed in this work will be a futuristic candidate to enhance the filtration efficiency of dye

pollutants from textile waste water treatment towards Zero Liquid Discharge process. Further studies on the effect of temperature, contact time, pH etc for adsorption, and effect of concentration of catalyst, mineralisation will shed more light on understanding the benchmarking samples in the independent process of photocatalysis/ adsorption.

### **Acknowledgement:**

Satheesh Krishnamurthy acknowledges Recycling Lithium ion batteries for a sustainable technological and economic development (ReListed) DSTUKIERI-2018-19-008, Royal Society IES\R2\170272 and Royal Academy of Engineering for the funding support. Sudhagar Pitchaimuthu acknowledges European Regional Development Grant for providing Ser Cymru-II Rising Star Fellowship through Welsh Government (80761-SU-102 -West).

### **REFERENCES**

- Ai, K., Ruan, C., Shen, M., Lu, L., 2016. MoS<sub>2</sub>Nanosheets with Widened Interlayer Spacing for High-Efficiency Removal of Mercury in Aquatic Systems. *Advanced Functional Materials* 26, 5542-5549.
- Alomar, M., Liu, Y., Chen, W., Fida, H., 2019. Controlling the growth of ultrathin MoS<sub>2</sub> nanosheets/CdS nanoparticles by two-step solvothermal synthesis for enhancing photocatalytic activities under visible light. *Applied Surface Science* 480, 1078-1088.
- Bhatia, S.C., 2017. *Pollution Control in Textile Industry*. WPI Publishing.
- Chang, K., Chen, W., 2011. Single-layer MoS<sub>2</sub>/graphene dispersed in amorphous carbon: towards high electrochemical performances in rechargeable lithium ion batteries. *Journal of Materials Chemistry* 21, 17175.
- Chin, M., Cisneros, C., Stephanie, Vargas, K.M., Ishihara, K.M., Tian, F., 2018. Rhodamine B degradation by nanosized zeolitic imidazolate framework-8 (ZIF-8). *RSC Advances* 8, 26987-26997.
- Choi, H.C., Jung, Y.M., Kim, S.B., 2005. Size effects in the Raman spectra of TiO<sub>2</sub> nanoparticles. *Vibrational Spectroscopy* 37, 33-38.

Coto, M., Divitini, G., Dey, A., Krishnamurthy, S., Ullah, N., Ducati, C., Kumar, R.V., 2017. Tuning the properties of a black TiO<sub>2</sub>-Ag visible light photocatalyst produced by a rapid one-pot chemical reduction. *Materials Today Chemistry* 4, 142-149.

Dhandayuthapani, T., Sivakumar, R., Ilangovan, R., Gopalakrishnan, C., Sanjeeviraja, C., Sivanantharaja, A., Hari Krishna, R., 2018. Efficient electrochromic performance of anatase TiO<sub>2</sub> thin films prepared by nebulized spray deposition method. *Journal of Solid State Electrochemistry* 22, 1825-1838.

Długosz, M., Kwiecień, A., Żmudzki, P., Bober, B., Krzek, J., Bialczyk, J., Nowakowska, M., Szczubiałka, K., 2015. A hybrid adsorbent/visible light photocatalyst for the abatement of microcystin-LR in water. *Chemical Communications* 51, 7649-7652.

Duong, D.L., Yun, S.J., Lee, Y.H., 2017. van der Waals Layered Materials: Opportunities and Challenges. *ACS Nano* 11, 11803-11830.

Fanourakis, S.K., Peña-Bahamonde, J., Bandara, P.C., Rodrigues, D.F., 2020. Nano-based adsorbent and photocatalyst use for pharmaceutical contaminant removal during indirect potable water reuse. *npj Clean Water* 3, 1.

Gan, X., Lee, L.Y.S., Wong, K.-y., Lo, T.W., Ho, K.H., Lei, D.Y., Zhao, H., 2018. 2H/1T Phase Transition of Multilayer MoS<sub>2</sub> by Electrochemical Incorporation of S Vacancies. *ACS Applied Energy Materials* 1, 4754-4765.

Geng, X., Sun, W., Wu, W., Chen, B., Al-Hilo, A., Benamara, M., Zhu, H., Watanabe, F., Cui, J., Chen, T.-P., 2016. Pure and stable metallic phase molybdenum disulfide nanosheets for hydrogen evolution reaction. *Nature Communications* 7, 10672.

Han, M., Zhu, S., Lu, S., Song, Y., Feng, T., Tao, S., Liu, J., Yang, B., 2018. Recent progress on the photocatalysis of carbon dots: Classification, mechanism and applications. *Nano Today* 19, 201-218.

Han, S., Liu, K., Hu, L., Teng, F., Yu, P., Zhu, Y., 2017. Superior Adsorption and Regenerable Dye Adsorbent Based on Flower-Like Molybdenum Disulfide Nanostructure. *Scientific Reports* 7, 43599.

He, H., Lin, J., Fu, W., Wang, X., Wang, H., Zeng, Q., Gu, Q., Li, Y., Yan, C., Tay, B.K., Xue, C., Hu, X., Pantelides, S.T., Zhou, W., Liu, Z., 2016. MoS<sub>2</sub>/TiO<sub>2</sub> Edge-On Heterostructure for Efficient Photocatalytic Hydrogen Evolution. *Advanced Energy Materials* 6, 1600464.

Hermosilla, D., Merayo, N., Gascó, A., Blanco, Á., 2015. The application of advanced oxidation technologies to the treatment of effluents from the pulp and paper industry: a review. *Environmental Science and Pollution Research* 22, 168-191.

Ho, W., Yu, J.C., Lin, J., Yu, J., Li, P., 2004. Preparation and Photocatalytic Behavior of MoS<sub>2</sub> and WS<sub>2</sub> Nanocluster Sensitized TiO<sub>2</sub>. *Langmuir* 20, 5865-5869.

Kanakaraju, D., Ravichandar, S., Lim, Y.C., 2017. Combined effects of adsorption and photocatalysis by hybrid TiO<sub>2</sub>/ZnO-calcium alginate beads for the removal of copper. *J Environ Sci (China)* 55, 214-223.

Kim, J.H., Kim, T.H., Lee, H., Park, Y.R., Choi, W., Lee, C.J., 2016. Thickness-dependent electron mobility of single and few-layer MoS<sub>2</sub> thin-film transistors. *AIP Advances* 6, 065106.

Kou, J., Lu, C., Wang, J., Chen, Y., Xu, Z., Varma, R.S., 2017. Selectivity Enhancement in Heterogeneous Photocatalytic Transformations. *Chemical Reviews* 117, 1445-1514.

Kumar, N., Fosso-Kankeu, E., Ray, S.S., 2019. Achieving Controllable MoS<sub>2</sub> Nanostructures with Increased Interlayer Spacing for Efficient Removal of Pb(II) from Aquatic Systems. *ACS Applied Materials & Interfaces* 11, 19141-19155.

Li, B., Jiang, L., Li, X., Ran, P., Zuo, P., Wang, A., Qu, L., Zhao, Y., Cheng, Z., Lu, Y., 2017. Preparation of Monolayer MoS<sub>2</sub> Quantum Dots using Temporally Shaped Femtosecond Laser Ablation of Bulk MoS<sub>2</sub> Targets in Water. *Scientific Reports* 7.

Li, K., Zhong, Y., Luo, S., Deng, W., 2020. Fabrication of powder and modular H<sub>3</sub>PW<sub>12</sub>O<sub>40</sub>/Ag<sub>3</sub>PO<sub>4</sub> composites: Novel visible-light photocatalysts for ultra-fast degradation of organic pollutants in water. *Applied Catalysis B: Environmental* 278, 119313.

Li, Z., Meng, X., Zhang, Z., 2019. Equilibrium and kinetic modelling of adsorption of Rhodamine B on MoS<sub>2</sub>. *Materials Research Bulletin* 111, 238-244.

Lin, Y., Ren, P., Wei, C., 2019. Fabrication of MoS<sub>2</sub>/TiO<sub>2</sub> heterostructures with enhanced photocatalytic activity. *CrystEngComm* 21, 3439-3450.

Liu, C., Wang, L., Tang, Y., Luo, S., Liu, Y., Zhang, S., Zeng, Y., Xu, Y., 2015a. Vertical single or few-layer MoS<sub>2</sub> nanosheets rooting into TiO<sub>2</sub> nanofibers for highly efficient photocatalytic hydrogen evolution. *Applied Catalysis B: Environmental* 164, 1-9.

Liu, H., Lv, T., Zhu, C., Su, X., Zhu, Z., 2015b. Efficient synthesis of MoS<sub>2</sub> nanoparticles modified TiO<sub>2</sub> nanobelts with enhanced visible-light-driven photocatalytic activity. *Journal of Molecular Catalysis A: Chemical* 396, 136-142.

Liu, Y., Li, Y., Peng, F., Lin, Y., Yang, S., Zhang, S., Wang, H., Cao, Y., Yu, H., 2019. 2H- and 1T- mixed phase few-layer MoS<sub>2</sub> as a superior to Pt co-catalyst coated on TiO<sub>2</sub> nanorod arrays for photocatalytic hydrogen evolution. *Applied Catalysis B: Environmental* 241, 236-245.

Mehta, M., Kodan, N., Kumar, S., Kaushal, A., Mayrhofer, L., Walter, M., Moseler, M., Dey, A., Krishnamurthy, S., Basu, S., Singh, A.P., 2016. Hydrogen treated anatase TiO<sub>2</sub>: a new

experimental approach and further insights from theory. *Journal of Materials Chemistry A* 4, 2670-2681.

Mehta, M., Singh, A.P., Kumar, S., Krishnamurthy, S., Wickman, B., Basu, S., 2018. Synthesis of MoS<sub>2</sub>-TiO<sub>2</sub> nanocomposite for enhanced photocatalytic and photoelectrochemical performance under visible light irradiation. *Vacuum* 155, 675-681.

Mohammadreza Miraboutalebi, S., Peydayesh, M., Bagheri, M., Mohammadi, T., 2020. Polyacrylonitrile/ $\alpha$ -Fe<sub>2</sub>O<sub>3</sub> Hybrid Photocatalytic Composite Adsorbents for Enhanced Dye Removal. *Chemical Engineering & Technology* 43, 1214-1223.

Muthu, S.S., 2017. *Sustainability in the Textile Industry*. Springer.

Park, M., Anumol, T., Simon, J., Zraick, F., Snyder, S.A., 2017. Pre-ozonation for high recovery of nanofiltration (NF) membrane system: Membrane fouling reduction and trace organic compound attenuation. *Journal of Membrane Science* 523, 255-263.

Perera, S.D., Mariano, R.G., Vu, K., Nour, N., Seitz, O., Chabal, Y., Balkus, K.J., 2012. Hydrothermal Synthesis of Graphene-TiO<sub>2</sub> Nanotube Composites with Enhanced Photocatalytic Activity. *ACS Catalysis* 2, 949-956.

Qi, Y., Wang, N., Xu, Q., Li, H., Zhou, P., Lu, X., Zhao, G., 2015. A green route to fabricate MoS<sub>2</sub> nanosheets in water-ethanol-CO<sub>2</sub>. *Chemical Communications* 51, 6726-6729.

Raja, R., Sudhagar, P., Devadoss, A., Terashima, C., Shrestha, L.K., Nakata, K., Jayavel, R., Ariga, K., Fujishima, A., 2015. Pt-free solar driven photoelectrochemical hydrogen fuel generation using 1T MoS<sub>2</sub> co-catalyst assembled CdS QDs/TiO<sub>2</sub> photoelectrode. *Chemical Communications* 51, 522-525.

Salleh, M.A.M., Mahmoud, D.K., Karim, W.A.W.A., Idris, A., 2011. Cationic and anionic dye adsorption by agricultural solid wastes: A comprehensive review. *Desalination* 280, 1-13.

Singh, A.P., Kodan, N., Mehta, B.R., Dey, A., Krishnamurthy, S., 2016. In-situ plasma hydrogenated TiO<sub>2</sub> thin films for enhanced photoelectrochemical properties. *Materials Research Bulletin* 76, 284-291.

Tao, R., Li, X., Li, X., Liu, S., Shao, C., Liu, Y., 2020. Discrete heterojunction nanofibers of BiFeO<sub>3</sub>/Bi<sub>2</sub>WO<sub>6</sub>: Novel architecture for effective charge separation and enhanced photocatalytic performance. *Journal of Colloid and Interface Science* 572, 257-268.

Vergili, I., Kaya, Y., Sen, U., Gönder, Z.B., Aydiner, C., 2012. Techno-economic analysis of textile dye bath wastewater treatment by integrated membrane processes under the zero liquid discharge approach. *Resources, Conservation and Recycling* 58, 25-35.

Vimonses, V., Jin, B., Chow, C.W.K., Saint, C., 2010. An adsorption–photocatalysis hybrid process using multi-functional-nanoporous materials for wastewater reclamation. *Water Research* 44, 5385-5397.

Vrubel, H., Merki, D., Hu, X., 2012. Hydrogen evolution catalyzed by MoS<sub>3</sub> and MoS<sub>2</sub> particles. *Energy & Environmental Science* 5, 6136-6144.

Wang, D., Zhang, X., Bao, S., Zhang, Z., Fei, H., Wu, Z., 2017. Phase engineering of a multiphasic 1T/2H MoS<sub>2</sub> catalyst for highly efficient hydrogen evolution. *Journal of Materials Chemistry A* 5, 2681-2688.

Wang, S., Zhang, D., Li, B., Zhang, C., Du, Z., Yin, H., Bi, X., Yang, S., 2018. Ultrastable In-Plane 1T-2H MoS<sub>2</sub> Heterostructures for Enhanced Hydrogen Evolution Reaction. *Advanced Energy Materials* 8, 1801345.

Weber, T., Muijsers, J.C., Van Wolput, J.H.M.C., Verhagen, C.P.J., Niemantsverdriet, J.W., 1996. Basic Reaction Steps in the Sulfidation of Crystalline MoO<sub>3</sub> to MoS<sub>2</sub>, As Studied by X-ray Photoelectron and Infrared Emission Spectroscopy. *The Journal of Physical Chemistry* 100, 14144-14150.

Wu, P.-R., Liu, Z., Cheng, Z.-L., 2019. Hydrothermal-assisted shearing exfoliation for few-layered MoS<sub>2</sub> nanosheets. *RSC Advances* 9, 17016-17024.

Xi, F., Bogdanoff, P., Harbauer, K., Plate, P., Höhn, C., Rappich, J., Wang, B., Han, X., Van De Krol, R., Fiechter, S., 2019. Structural Transformation Identification of Sputtered Amorphous MoS<sub>x</sub> as an Efficient Hydrogen-Evolving Catalyst during Electrochemical Activation. *ACS Catalysis* 9, 2368-2380.

Xiang, Q., Yu, J., Jaroniec, M., 2012. Synergetic Effect of MoS<sub>2</sub> and Graphene as Cocatalysts for Enhanced Photocatalytic H<sub>2</sub> Production Activity of TiO<sub>2</sub> Nanoparticles. *Journal of the American Chemical Society* 134, 6575-6578.

Xiao, X., Wang, Y., Cui, B., Zhang, X., Zhang, D., Xu, X., 2020. Preparation of MoS<sub>2</sub> nanoflowers with rich active sites as an efficient adsorbent for aqueous organic dyes. *New Journal of Chemistry* 44, 4558-4567.

Xu, J., Zhang, J., Zhang, W., Lee, C.-S., 2017. Interlayer Nanoarchitectonics of Two-Dimensional Transition-Metal Dichalcogenides Nanosheets for Energy Storage and Conversion Applications. *Advanced Energy Materials* 7, 1700571.

Yang, H., Yuan, H., Hu, Q., Liu, W., Zhang, D., 2020. Synthesis of mesoporous C/MoS<sub>2</sub> for adsorption of methyl orange and photo-catalytic sterilization. *Applied Surface Science* 504, 144445.

Yang, H.G., Zeng, H.C., 2004. Preparation of Hollow Anatase TiO<sub>2</sub>Nanospheres via Ostwald Ripening. *The Journal of Physical Chemistry B* 108, 3492-3495.

Zhou, W., Yin, Z., Du, Y., Huang, X., Zeng, Z., Fan, Z., Liu, H., Wang, J., Zhang, H., 2013a. Synthesis of Few-Layer MoS<sub>2</sub> Nanosheet-Coated TiO<sub>2</sub> Nanobelt Heterostructures for Enhanced Photocatalytic Activities. *Small* 9, 140-147.

Zhou, W., Yin, Z., Du, Y., Huang, X., Zeng, Z., Fan, Z., Liu, H., Wang, J., Zhang, H., 2013b. Synthesis of Few-Layer MoS<sub>2</sub>Nanosheet-Coated TiO<sub>2</sub>Nanobelt Heterostructures for Enhanced Photocatalytic Activities. *Small* 9, 140-147.

Zhou, X., Lickleder, M., Schmuki, P., 2016. Thin MoS<sub>2</sub> on TiO<sub>2</sub> nanotube layers: An efficient co-catalyst/harvesting system for photocatalytic H<sub>2</sub> evolution. *Electrochemistry Communications* 73, 33-37.